University of Baghdad
College of Engineering
JOURNAL OF ENGINEERING

Journal of Engineering

journal homepage: www.jcoeng.edu.iq

Volume 32 Number 9 September 2026

Experimental and CFD Investigation of Wind-Induced Pressures on an 8° Gable Roof with Different Roof Opening Configurations

Ashraf Hameed Alsalmani [1, 2, *], **Salah R. Al-Zaidee** [2]

[1]Office of the Speaker of the Iraqi Council of Representatives, Baghdad, Iraq
[2]Department of Civil Engineering, College of Engineering, University of Baghdad, Baghdad, Iraq

ABSTRACT

The research aims at studying the wind-induced pressure on an 8° low-slope gable roof by means of wind tunnel tests and ANSYS Fluent simulation analysis. Direct pressure measurements were obtained from the experimental tests, and the resulting pressure distribution and aerodynamic flow were interpreted by the numerical model. The four roof configurations examined were a closed roof, a single opening, two openings and four openings. These cases were then tested experimentally under the same conditions in an open-circuit wind tunnel at the College of Engineering at the University of Baghdad with a fixed wind velocity of 38 m/s. Pressure coefficients were calculated from the pressure taps located over the windward wall, leeward wall and gable roof surfaces. A steady, incompressible RANS formulation numerical model was then constructed in ANSYS Fluent 2025 R1 with the standard k–ε turbulence model. Increasing the number of openings on the roof resulted in improved interaction between the external separated flow and the internal air volume and resulted in a noticeable redistribution of the pressure over the roof surface. The CFD results were compared with the experimental measurements, and the results were very good, with a high $R^2 = 0.996$, an $RMSE = 0.069$ and a $ME = 0.051$. Based on the results, it can be concluded that the openings of a roof can have a significant impact on the aerodynamic pressure response of low-rise gable roofs and that the openings should be taken into account when assessing roof pressures due to wind.

Keywords: Computational fluid dynamics (CFD), Gable roof, Pressure coefficient, Roof openings, Wind engineering.

1. INTRODUCTION

The sensitivity of low-rise industrial and agricultural buildings to the pressures imposed on their roofs by wind forces is particularly high, due to separation of the wind flow in the area around sharp roof edges, creating strong local suction **(Simiu and Scanlan, 1996).**
The suction can also be the most important load on light weight cladding, fasteners, eave areas, ridge areas, and other roof features, more so than the overall wind load on the building

*Corresponding author
Peer review under the responsibility of University of Baghdad.
https://doi.org/10.31026/j.eng.2026.09.09
This is an open access article under the CC BY 4 license (http://creativecommons.org/licenses/by/4.0/).
Article received: 20/06/2026
Article revised: 19/07/2026
Article accepted: 20/07/2026
Article published: 01/09/2026

itself. It is therefore important to assess local pressure coefficients for wind-induced roof uplift and cladding performance. This study concerns with an 8° low rise gable roof and the pressure coefficients generated over the roof surfaces and walls **(Aynsley et al., 1977; Stathopoulos, 1984; Dyrbye and Hansen, 1997; Tieleman, 2003).**

Aerodynamic behavior is also influenced by the roof opening. The wind-pressure pattern over a low-rise gable roof is generated by the interplay between indoor/outdoor geometry and incoming wind. As the flow reaches the windward wall, it stagnates, and another portion of the flow is accelerated and separates near the roof edges, as it flows over the inclined roof surface. The mechanism results in positive pressure on the windward wall and negative pressure over the roof surface and leeward area (as illustrated in **Fig. 1**) **(Cook, 1985; Holmes, 2020)**

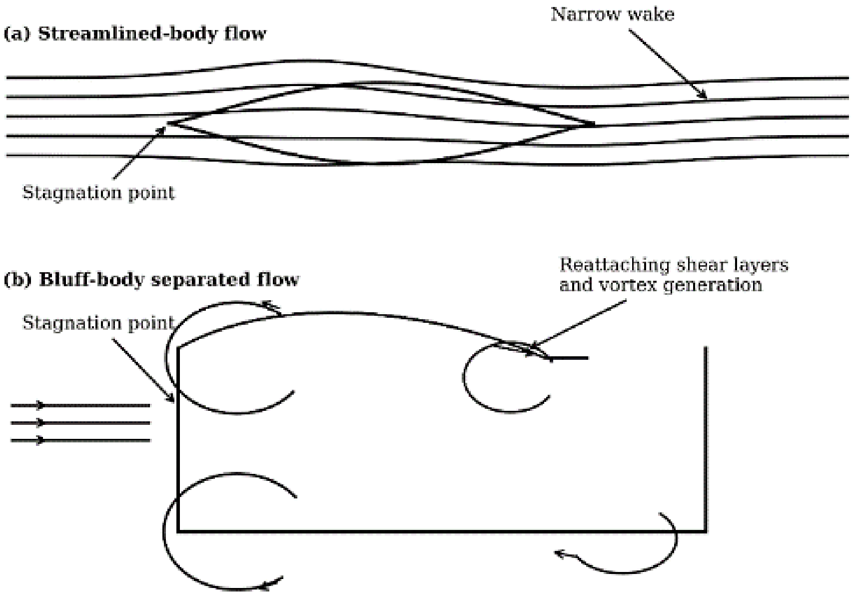

Figure 1. Schematic representation of the main aerodynamic mechanisms controlling roof pressure, including stagnation, flow separation, shear-layer reattachment, wake formation, and vortex generation.

So, the roof pressure field should not be taken as uniform, as there can be local suction over the edge of the roof, which may be more significant aerodynamically than the aerodynamic demand of the wind on the whole building. This flow behavior is altered by all roof openings, as they allow for interaction between the separate flow from the outside and the volume of air inside. This interaction can lead to a redistribution of the pressure around the opening areas and alter the local suction response above the roof **(Ginger et al., 1997; Kopp et al., 2008; Holmes and Ginger, 2012).** Therefore, roof openings mustn't be treated as architectural or service elements only, but also as aerodynamic flow paths, particularly when they are situated in high-suction roof areas **(Kopp et al., 2008; Demir and Aktepe, 2025).**
The aerodynamic response of the gable-roof model was evaluated through wind tunnel testing and CFD simulation in ANSYS Fluent **(Al Salmani et al., 2019).** The experimental measurements provided local pressure data, while the CFD model was used to interpret the associated pressure distribution, velocity variation, flow separation, streamline behavior, and wake development around the roof **(Cermak, 2003; Blocken, 2014).** This combined approach is particularly useful for roof-opening problems because pressure taps quantify the local aerodynamic response, whereas CFD explains how the external separated flow interacts with the internal cavity through the openings.

CFD predictions of separated flow around bluff bodies are sensitive to the computational-domain dimensions, mesh resolution, boundary conditions, near-wall treatment, and turbulence-model formulation. Accordingly, the numerical model was validated against the wind-tunnel measurements before it was used to interpret the aerodynamic mechanisms associated with the investigated roof-opening configurations **(Murakami, 1997; Tominaga et al., 2008; Lateb et al., 2013).**

Wind-induced pressures on low-rise buildings have been widely investigated. Nevertheless, comparatively few experimental and numerical studies have considered low-pitched gable roofs with multiple roof openings, particularly when the reference wind velocity is established from long-term local wind records. The present study therefore examines the aerodynamic response of an 8° low-rise gable roof under four configurations: a closed roof, one opening, two openings, and four openings. Wind-tunnel tests were performed at a reference velocity of 38 m/s, obtained from an extreme-value analysis of Baghdad wind-speed records. Surface pressures were measured at 34 pressure taps distributed over the roof and wall surfaces.

A corresponding CFD model was developed in ANSYS Fluent 2025 R1 to reproduce the experimental conditions and supplement the measured data with detailed flow-field information. The investigation addresses surface-pressure coefficients, local roof suction, pressure redistribution, airflow exchange through the openings, and downstream wake development. The numerical predictions were assessed through direct comparison with the wind-tunnel measurements. The resulting analysis provides a clearer understanding of how the number of roof openings modifies the aerodynamic pressure response of low-rise gable roofs and supports the assessment of wind loads on similar roof systems.

2. MATERIALS AND METHOD

2.1 Wind Tunnel Facility and Reference Flow Condition

The tests were carried out in an open-circuit subsonic wind tunnel at the College of Engineering, University of Baghdad. The test section is 0.70 m wide, 0.70 m high, and 1.50 m long. This size was enough to place the roof model inside the tunnel with side clearance for the airflow. **Fig. 2** shows the tunnel layout, the model position, and the actual facility. Airflow was supplied by a downstream axial fan with a 55 kW motor. The fan speed was controlled by a Delta C2000+ VFD. The speed was adjusted before taking the pressure readings **(Cermak, 2003; Tieleman, 2003).**

A reference wind velocity of 38 m/s was adopted in this study. This value was selected from the extreme-value analysis of nearly 35 years of Baghdad wind-speed records and was used in both the wind tunnel tests and CFD simulations **(Palutikof et al., 1999)**. The corresponding dynamic pressure was calculated using Eq. (1) **(Solari, 1993):**

$$q = \frac{1}{2}\rho V^2 \tag{1}$$

where q is the dynamic pressure, ρ is the air density, and V is the reference wind velocity **(White, 2016)**. For $\rho = 1.182$ kg/m^3 and $V = 38\ m/s$. The resulting dynamic pressure is approximately 854 Pa. This value was used as the reference pressure for converting measured surface pressures into non-dimensional pressure coefficients and for maintaining consistency between the experimental and numerical analyses **(Holmes, 2020; ASCE, 2022)**.

A pitot static tube and a Dwyer Series 475 Mark II digital manometer were used for checking the reference flow. The fan speed fixed up the velocity to reach the dynamic pressure of 854 Pa. **Figs. 3 and 4** show the measuring and control devices used in this step. The pressure readings were then taken under the same wind conditions for all roof-opening cases **(Cermak, 2003; Tieleman, 2003).**

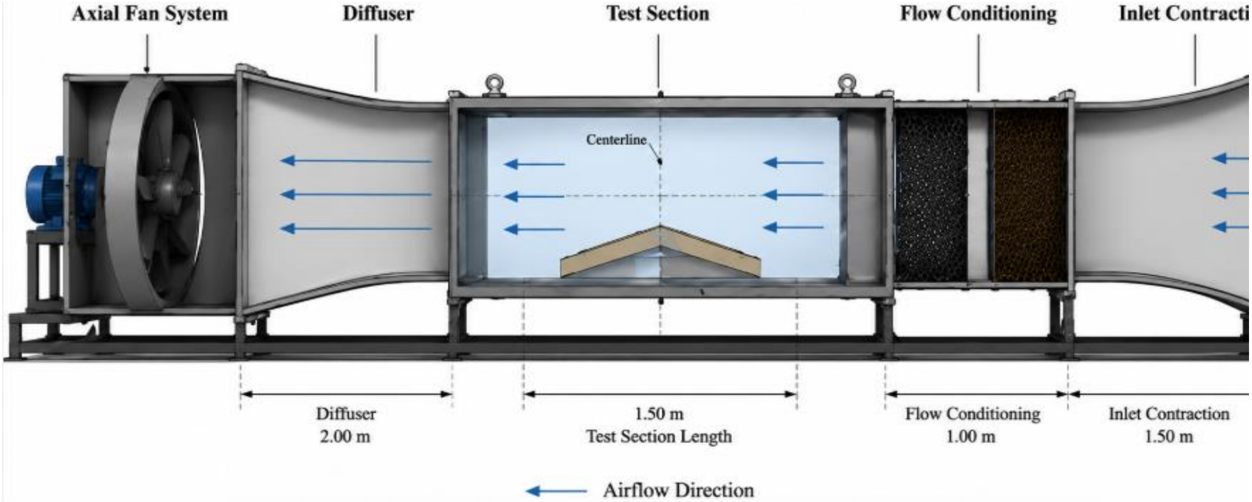

(a)

(b)

Figure 2. Open-circuit wind tunnel used in the experimental investigation: (a) schematic layout of the tunnel components and roof-model position inside the test section; (b) actual wind tunnel facility at the Department of Aerospace Engineering, University of Baghdad.

(a)

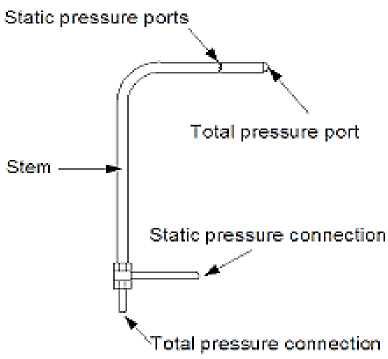

(b)

Figure 3. Reference-flow verification and control system: (a) Dwyer Series 475 Mark III digital differential manometer; (b) Pitot-static tube arrangement

Figure 4. Electrical control panel and Delta C2000+ Variable Frequency Drive.

2.2 Roof Model and Opening Configurations

The investigated model represents an 8° low-rise gable-roof structure. The same external roof geometry was maintained for all tested cases so that the aerodynamic influence of the roof openings could be evaluated without introducing additional changes in roof slope or building dimensions. The principal model dimensions were 0.35 m in width, 0.30 m in depth, 0.12 m in eave height, and 0.135 m in total height, as summarized in **Table 1** and shown in **Fig. 5**. Four roof-opening configurations were investigated: closed roof, one opening, two openings, and four openings. Each roof opening had square dimensions of 4 cm × 4 cm, and the openings were arranged on the roof surface to evaluate the influence of increasing roof discontinuity on pressure redistribution and internal–external airflow interaction**.**

Table 1. Principal geometric dimensions of the investigated 8° gable-roof model.

Description	Parameter	Value
Building width	B	0.35 m
Building depth	D	0.30 m
Eave height	h	0.12 m
Total height	H	0.135
Roof slope angle	α	8°

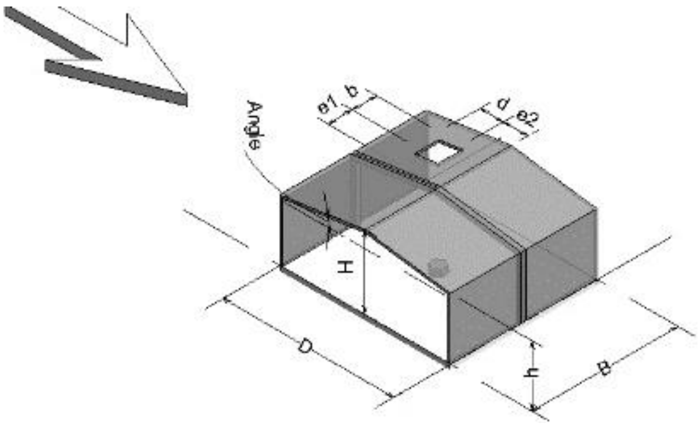

Figure 5. Three-dimensional geometry and principal dimensions of the investigated 8° gable-roof model.

As shown in **Fig. 6**, between the closed and open roof cases, four configurations were presented together to allow direct comparison. Preserving the same external dimensions for all configurations ensured that the practical aerodynamic changes were mainly related to the number of roof openings rather than unrelated geometric changes **(Li et al., 2025; Demir and Aktepe, 2025)**.

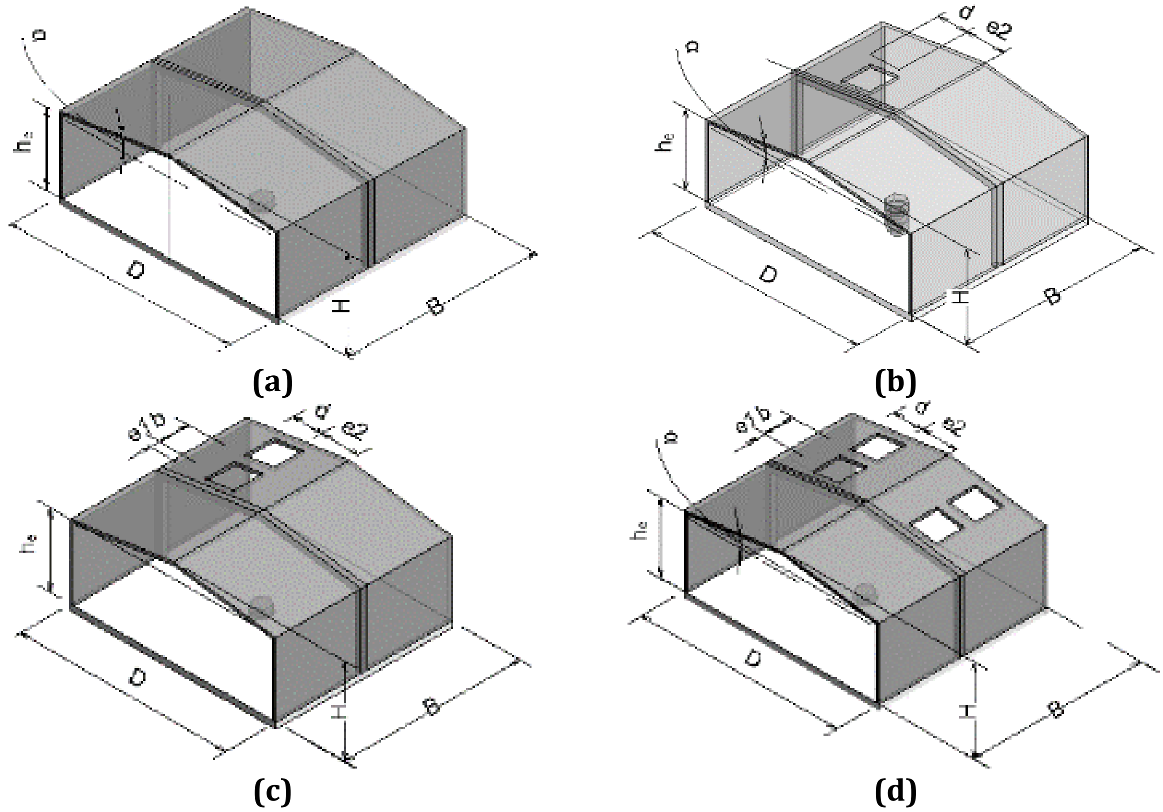

Figure 6. Geometric definition of the roof-opening configurations: (a) closed roof; (b) one opening; (c) two openings; and (d) four openings. B and D represent the building plan width and length, respectively; H is the eave height; h is the roof rise; b and d are the roof-opening width and length, respectively; and e_1 and e_2 denote the distances from the roof opening to the roof ridge and roof edge, respectively.

2.3 Blockage Ratio and Reynolds Number Similarity

The model position inside the wind tunnel was checked with the available test-section area then the pressure measurements were started. The roof model was mounted at the center of the 0.70 m × 0.70 m section, leaving approximately 0.20 m clearance on both sides. As shown in **Fig. 7**, this placement provided enough lateral space for the flow to pass around the model while keeping the tested cases under the same geometric conditions. The blockage ratio was slightly higher than the commonly recommended 10% value; however, this limitation affects all opening configurations in the same manner because the model position, tunnel dimensions, and reference velocity were not changed during the tests. Therefore, the comparison among the closed, one-opening, two-opening, and four-opening cases was treated as a consistent comparative assessment **(Cermak, 2003; Tieleman, 2003)**.

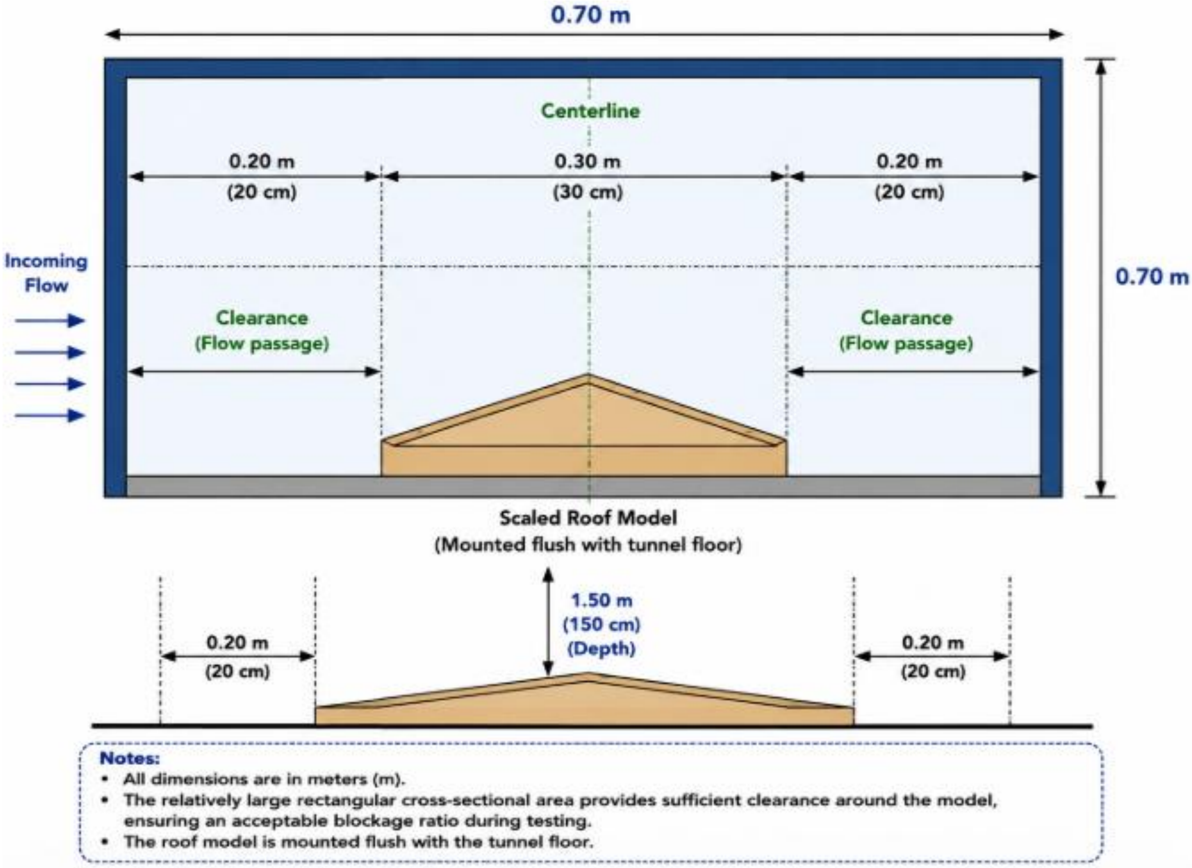

Figure 7. Wind tunnel blockage representation and geometric arrangement of the roof model inside the test section.

The blockage ratio was calculated using Eq. (2):

$$\beta = \frac{A_m}{A_t} \tag{2}$$

where β is the blockage ratio, A_m is the projected frontal area of the model normal to the airflow, and A_t is the cross-sectional area of the wind tunnel test section. The test-section area was calculated as $0.70\,m \times 0.70\,m = 0.49\,m^2$. This parameter was included to document the geometric relationship between the roof model and the available flow area inside the tunnel and to support the interpretation of the measured pressure coefficients under the adopted experimental arrangement **(Cermak, 2003; Tieleman, 2003).**

The Reynolds number was calculated to assess the aerodynamic similarity of the experimental condition **(Munson et al., 2013; Fox et al., 2015).** Using the reference velocity of 38 m/s, air density of 1.182 kg/m^3, dynamic viscosity of 1.81×10^{-5} Pa·s, and characteristic model height of 0.1669 m, the Reynolds number was obtained from Eq. (3):

$$R_e = \frac{\rho V H}{\mu} \tag{3}$$

where R_e is the Reynolds number, V is the reference wind velocity, ρ is the air density, H is the model height, and μ is the dynamic viscosity of air. The number of Reynolds was about 4.13×10^5 ,it's suitable for sharp-edged bluff-body flow, as shown in **Fig. 8.** Therefore, the test condition was used for comparing the measured pressure coefficients with the CFD results **(Lee, 1975; Melbourne, 1979)**.

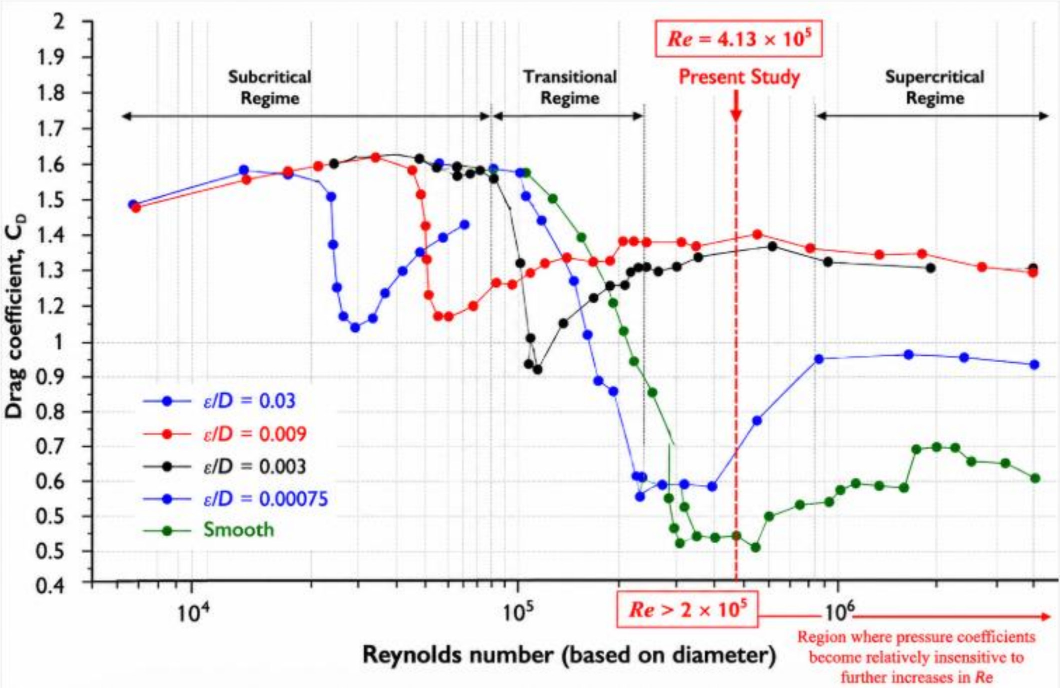

Figure 8. Reynolds-number behavior for bluff-body aerodynamic flow.

2.4 Pressure Tap Layout and Measurement System

Surface pressure was recorded at 34 locations on the model. Eight pressure taps were installed on the windward wall, eight on the leeward wall, and eighteen on the two roof slopes. The tap positions were selected according to the expected aerodynamic response of the model, with closer attention given to the windward roof edge, the ridge region, the vicinity of the roof openings, and the wall surface. The selected locations covered the regions where the largest pressure changes were expected, particularly near the windward edge, ridge, roof openings, and wall surfaces. This arrangement was used unchanged for the closed roof and for the one-, two- and four-opening configurations so that the measured responses could be compared on the same basis. Each pressure tap was connected to the acquisition system by a flexible tube routed through the interior of the model, as illustrated in **Fig. 9**. Keeping the tubes inside the model prevented them from interfering with the approaching airflow or changing the exposed roof geometry during testing **(Cermak, 2003; Tieleman, 2003)**.

The pressure signals were measured using miniature differential pressure sensors integrated into a custom-developed data acquisition system. **Fig. 10** shows the main components of the pressure-measurement system. The setup included miniature differential pressure sensors, a custom acquisition unit, and a computer used for recording and processing the measured signals. The recorded pressure differences were then converted to pressure coefficients using the reference dynamic pressure adopted for the experiments.

The pressure coefficient was calculated using Eq. (4):

$$C_p = \frac{P}{q} \tag{4}$$

In Eq. (4), C_p is the pressure coefficient, P is the measured pressure relative to the reference pressure, and q is the reference dynamic pressure. The use of non-dimensional pressure coefficients allowed direct comparison between wind tunnel measurements and CFD predictions for all roof-opening configurations **(ASCE, 2022)**.

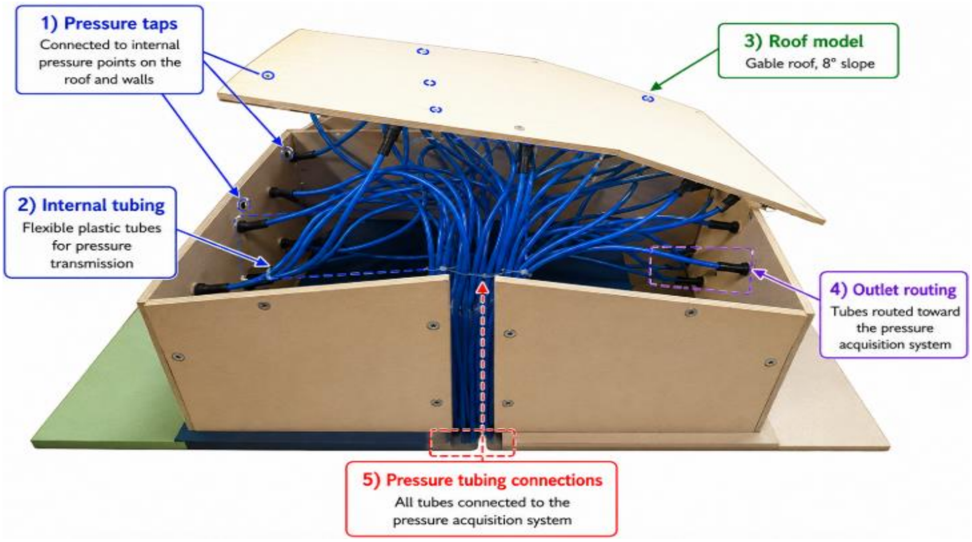

Figure 9. Pressure-tap locations and internal tubing connections within the gable-roof model.

Before recording each measurement, the airflow was allowed to stabilize under the prescribed test conditions. The pressure at each tap was then monitored for approximately 120 s, and the reported pressure coefficient was determined from the mean stabilized pressure value. This averaging procedure minimized the influence of short-term pressure fluctuations and provided representative mean pressure coefficients for comparison with the corresponding CFD predictions.

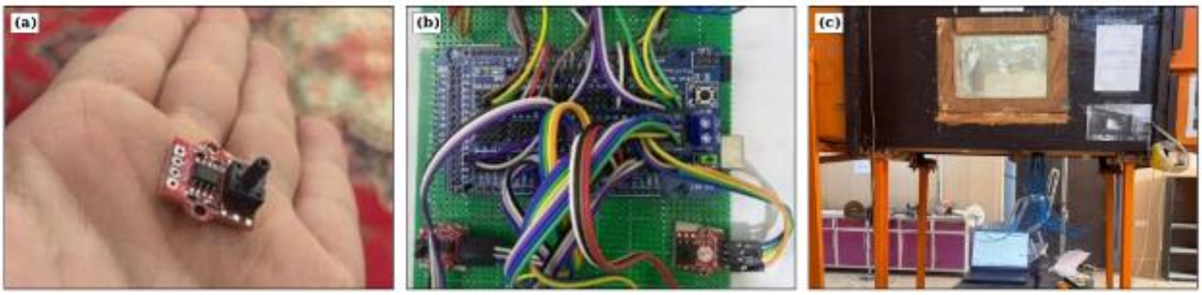

Figure 10. Pressure measurement and data acquisition system: (a) differential pressure sensors; (b) custom-developed acquisition unit; (c) computer-based recording and post-processing arrangement.

2.5 CFD Model and Numerical Setup

The numerical simulations were conducted to simulate the aerodynamic conditions of the wind tunnel experiments performed in this work in ANSYS Fluent 2025 R1. The computational domain was also established using the same dimensions of the test-section as were used in the experiments, i.e., width of 0.70 m, height of 0.70 m and length of 1.50 m, thus maintaining the same blockage environment, model position, and reference flow condition. The roof model was placed in the center of the computational domain, with the upstream boundary set to be a velocity inlet and the downstream boundary set as a pressure outlet, as seen in **Fig. 11.** The side walls, top wall, floor and roof-model surfaces were defined, based on the physical wind tunnel setup. It was decided to use this domain consistency to facilitate direct comparisons between the CFD pressure coefficients and the wind tunnel measurements **(Richards and Hoxey, 1993; Richards and Norris, 2011; Blocken, 2014)**.

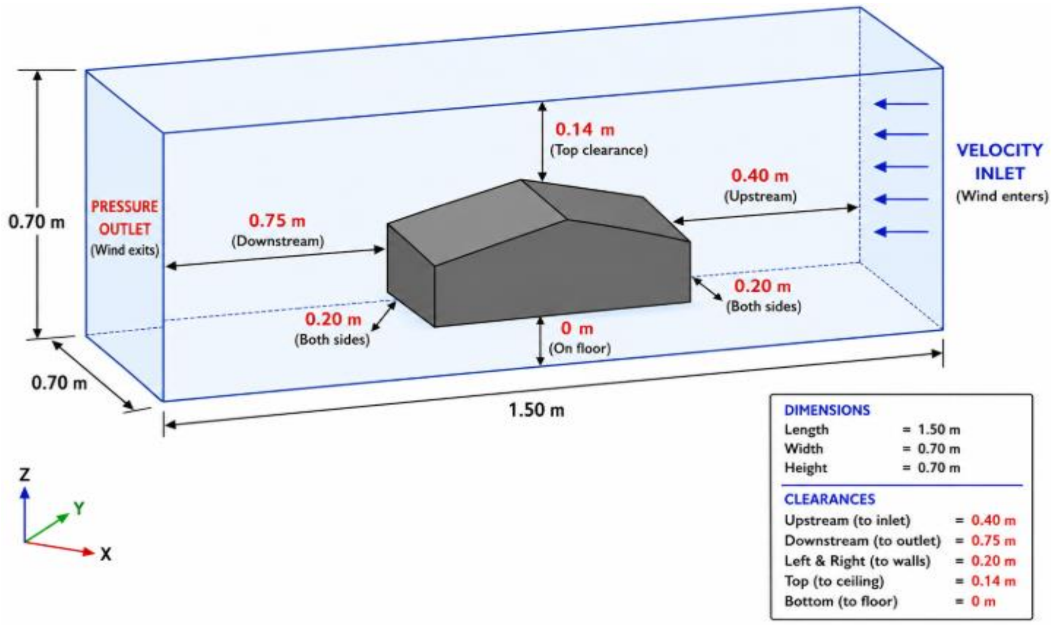

Figure 11. The CFD computational domain and boundary-condition arrangement reproduce the wind tunnel test section and roof-model position.

The flow field was assumed to be steady, three-dimensional, and incompressible, which is appropriate for the present low-speed wind-tunnel conditions. The mean flow around the roof model was simulated using the Reynolds-Averaged Navier–Stokes (RANS) equations, while the standard k–ε turbulence model was selected as the turbulence closure for the separated external flow around the sharp-edged roof geometry **(Launder and Spalding, 1974; ANSYS Inc., 2025)**.

The standard k–ε turbulence model was selected because it has been extensively validated and widely adopted for external aerodynamic simulations of sharp-edged bluff bodies, particularly for predicting mean aerodynamic quantities, including pressure distributions, under steady-state conditions. Several turbulence approaches were considered when defining the numerical model. SST k–ω and RNG k–ε can give additional information close to separated and recirculating regions, while LES can resolve time-dependent turbulent structures. These methods, however, demand finer grids and considerably longer calculations. The present CFD work was concerned mainly with the mean pressures measured on the roof and walls. On this basis, the standard k–ε model was used for the four opening arrangements. Its predictions were checked against the pressure-tap readings rather than accepted without experimental verification. The resulting comparison gave R^2 = 0.996, RMSE ≈ 0.069, and ME ≈ 0.051. A finite-volume formulation was used to solve the flow equations **(Ferziger and Peric, 2002; Versteeg and Malalasekera, 2007)**. In addition to the surface pressures available from the wind-tunnel tests, the CFD solution provided information about the flow in the surrounding and internal regions of the model **(Blocken, 2014)**.

A uniform velocity of 38 m/s was imposed at the inlet, while the downstream boundary was specified as a pressure outlet. The tunnel floor, ceiling, side walls, and model surfaces were treated as stationary no-slip walls to reproduce the experimental arrangement. The roof openings remained open within the fluid domain, allowing airflow between the internal space and the external region. The same geometry and reference-flow conditions were adopted in the numerical and experimental models, providing a consistent basis for direct comparison of the resulting pressure coefficients **(Richards and Hoxey, 1993; Franke et al., 2007)**. At the adopted reference velocity, the Reynolds number was approximately 4.13 × 10^5. This value lies within the range commonly associated with relatively weak Reynolds-number effects on the mean surface-pressure coefficients of sharp-edged low-rise bluff bodies **(Simiu and Scanlan, 1996; Stathopoulos et al., 2014)**.

Previous wind-engineering studies have shown that, beyond this range, the mean surface-pressure coefficients become relatively insensitive to further increases in Reynolds number. As illustrated in **Fig. 8**, the adopted Reynolds number falls within the Reynolds-independent region, indicating that the measured pressure coefficients are not expected to be significantly influenced by further increases in Reynolds number. Therefore, the adopted flow conditions were considered appropriate for the comparative aerodynamic assessment performed in the present study **(Simiu and Scanlan, 1996; Stathopoulos et al., 2014).**

The mesh was generated with unstructured tetrahedra, and additional refinement was applied in the region near the surface of the roof, near the roof opening edges, near the windward roof region, near the roof ridge and near the wake region. The locations were optimized to account for the main pressure gradients and separated-flow characteristics that were anticipated to be present around the sharp edges of the roof and around the boundaries of the openings. The grid density was increased around the model of the building (as illustrated in **Fig. 12**), and surface elements were reduced to high density in the regions that contained roof openings, for better local pressure variation extraction. For the steady RANS simulations, this mesh configuration gave a good compromise between the numerical resolution and the computational effort required **(Tominaga et al., 2008; ANSYS Inc., 2025).**

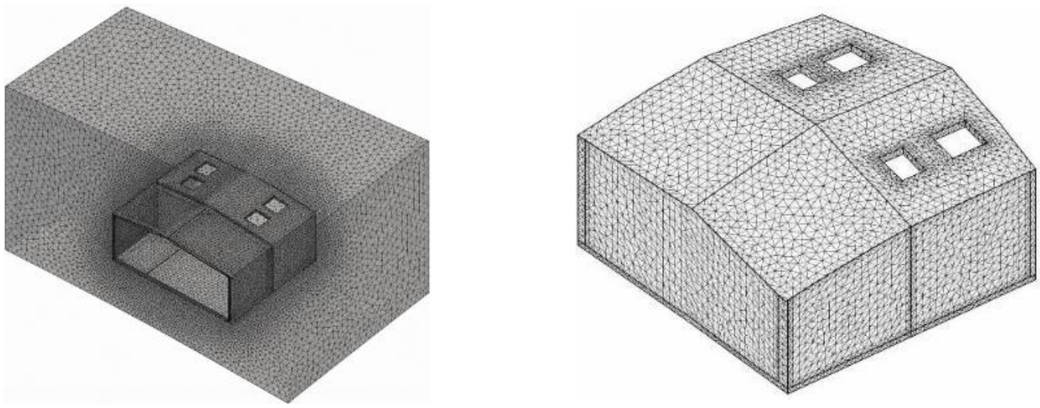

(a) **(b)**

Figure 12. Computational mesh used in the CFD simulation: (a) overall mesh distribution within the computational domain; (b) local surface mesh refinement around the gable-roof model and roof openings.

The calculations continued until the residuals reached the specified limits and the monitored roof pressures became nearly unchanged from one iteration to the next. A residual target of 10^{-3} was applied to the continuity, momentum, turbulent kinetic energy, and turbulence dissipation-rate equations. Convergence was not judged from the residual history alone; pressure values on selected roof and wall locations were also checked before the final results were exported. **Fig. 13**, shows the residual development during the solution process and indicates that a stable numerical state had been reached before extracting the pressure coefficients. Computed static pressures were then normalized using the same reference dynamic pressure adopted in the wind-tunnel analysis, which provided a consistent basis for direct comparison between the numerical and experimental results **(Blocken, 2014; ANSYS Inc., 2025).**

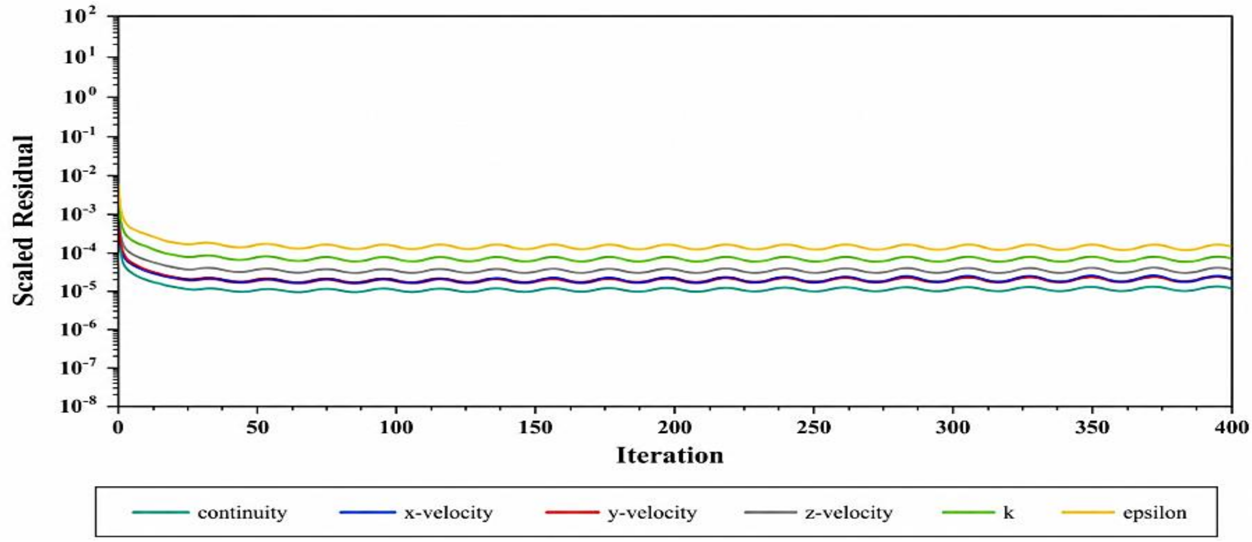

Figure 13. Residual convergence history was adopted for the CFD solution.

3. RESULTS AND DISCUSSION

Four roof conditions were examined for the 8° gable model: a closed roof and roofs containing one, two, or four openings. The experimental results are expressed in terms of wind-tunnel pressure coefficients, while the numerical results are presented through CFD pressure contours. Attention is given to the changes in roof suction, surface-pressure distribution, airflow through the openings, and wake development. The discussion considers the windward and leeward walls, the roof slopes, the windward roof edge, the ridge region, and the boundaries of the openings. This section first describes the general aerodynamic behavior of the investigated roof model and then discusses the pressure response for each opening configuration **(Kopp et al., 2008)**.

3.1 General Aerodynamic Behavior of the 8° Gable Roof

The general aerodynamic response of the 8° gable-roof model was controlled by the interaction between windward-wall stagnation, flow acceleration over the roof surface, separation near the windward roof edge, and wake formation behind the leeward side. Under the approaching flow, positive pressure developed mainly on the windward wall, while suction dominated the roof surfaces because the flow accelerated over the inclined roof and separated near the roof edges. As shown in **Fig. 14**, the flow first impinges on the windward wall and forms a stagnation region, then accelerates over the roof surface, separates near the roof edges, and develops a recirculating wake downstream of the building model. The maximum suction occurs near the windward roof edge and ridge-adjacent regions. The leeward roof and wall surfaces then show gradual pressure recovery as the separated flow reattaches and develops into the wake region. This pattern agrees with the aerodynamic behavior of sharp-edged low-rise buildings, where local roof suction is governed by edge separation, vortex formation, and flow instability near the roof perimeter **(Kawai and Nishimura, 1996; Holmes, 2020).**

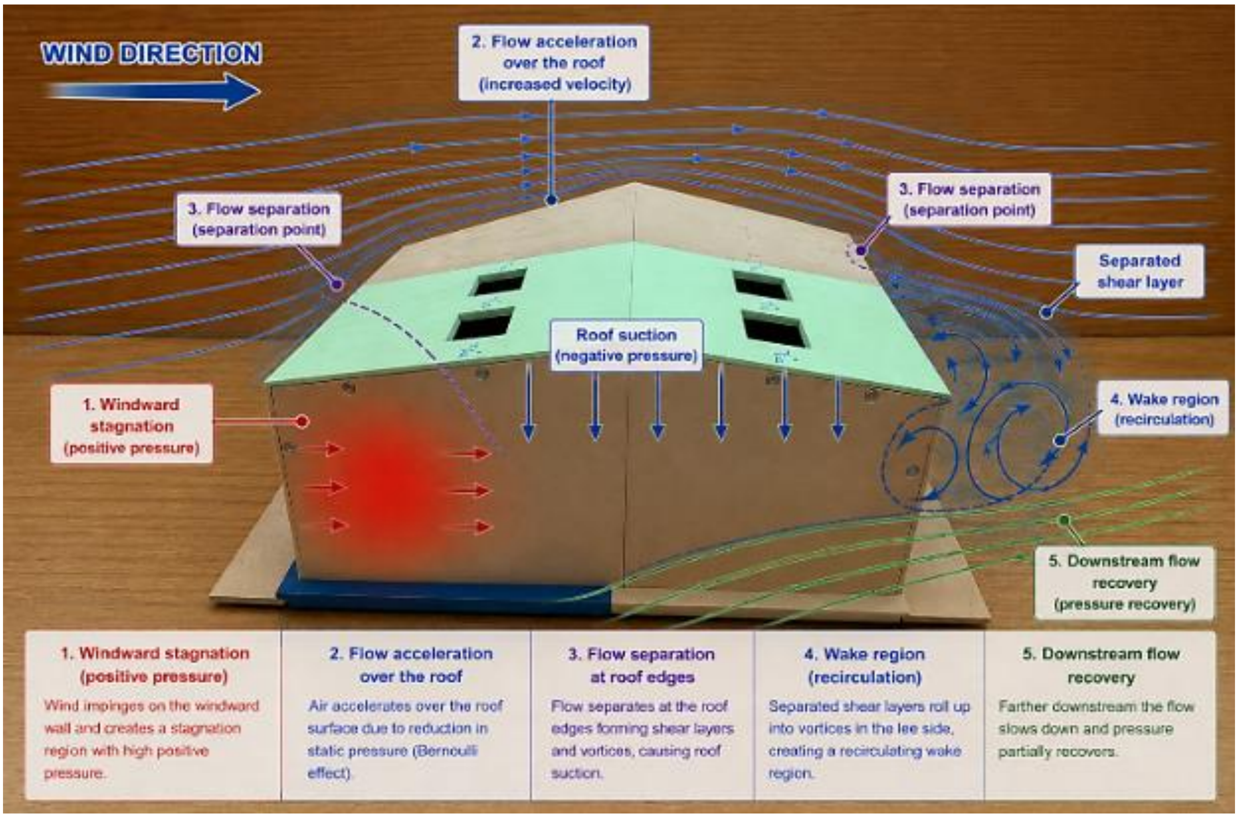

Figure 14. Principal airflow and pressure features around the 8° gable-roof model

3.2 Pressure-Field Response for Different Opening Configurations

The pressure contours in **Fig. 15** show a common feature in all four cases: the windward wall remained under positive pressure, whereas the roof surfaces were mainly subjected to suction. The closed roof produced the broadest continuous suction band across the two slopes. Adding one opening caused only a limited change around its immediate location. Most of the remaining roof retained a pressure pattern close to the closed-roof case. With two openings, the affected area became wider, and the differences were concentrated mainly along the opening edges.

The four-opening arrangement produced the largest change in the roof contour. The pressure field around the openings became less continuous, while the windward-wall pressure remained nearly the same as in the other configurations. Suction near the openings was also less concentrated than in the closed-roof case. This reduction may be attributed to the additional paths through which part of the pressure difference between the internal and external regions was relieved. Overall, the results indicate that the number of roof openings influences both the local pressures near the openings and the broader pressure pattern over the roof **(Li et al., 2025; Demir and Aktepe, 2025)**.

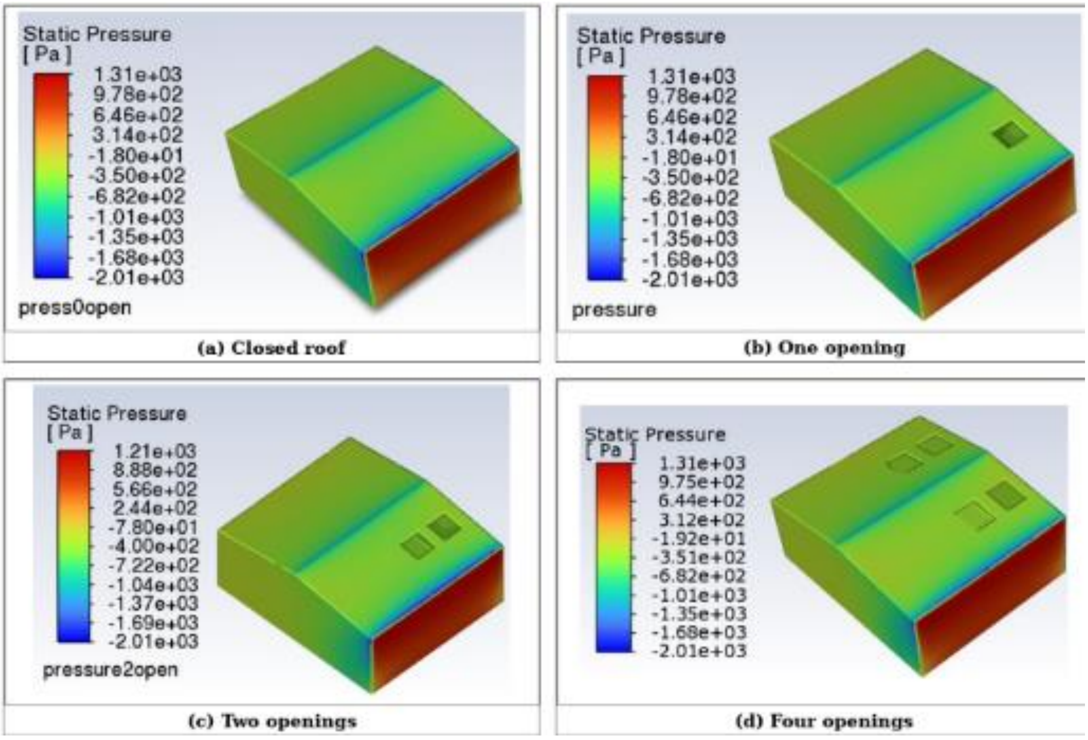

Figure 15. CFD pressure-field distribution for the 8° gable-roof model under different roof-opening configurations: (a) closed roof; (b) one opening; (c) two openings; (d) four openings.

In addition to the qualitative interpretation of the CFD pressure contours, the corresponding pressure-coefficient (Cp) distributions obtained from both the CFD simulations and the wind-tunnel measurements are presented in **Fig. 18**. The Cp comparison confirms that the numerical model reproduced the principal pressure characteristics observed experimentally, including the windward stagnation region, roof-edge suction, ridge-pressure variation, and the pressure redistribution associated with the different roof-opening configurations. Accordingly, the CFD pressure contours presented in **Fig. 15** should be interpreted together with the quantitative Cp comparisons shown in **Fig. 18**.

3.3 Velocity-Field Response for Different Opening Configurations

The velocity-magnitude contours presented in **Fig. 16** illustrate the influence of roof openings on the airflow distribution around the investigated roof configurations. In all cases, the incoming flow accelerated as it approached the windward roof edge, producing a high-velocity region above the roof surface as the boundary layer separated from the leading edge. This acceleration was accompanied by a corresponding reduction in static pressure, consistent with the pressure-field distributions presented in **Fig. 15**.
The closed model showed an uninterrupted external flow field. High velocity gradients appeared above the windward roof slope and within the separate layer over the roof. The introduction of one opening produced only a local disturbance, and the wider external pattern remained close to that of the closed case. For the models with two and four openings, the contour pattern changed more clearly near the roof openings. Velocity differences were concentrated around the opening edges, while the high-speed region above the roof became more dispersed.

This behavior suggests that the openings altered the path of the airflow and redistributed part of the flow through the internal space. It is preferable to interpret this as a change in airflow path and local velocity distribution rather than as dissipation of external kinetic energy, since kinetic-energy dissipation cannot be established from velocity-magnitude contours alone.

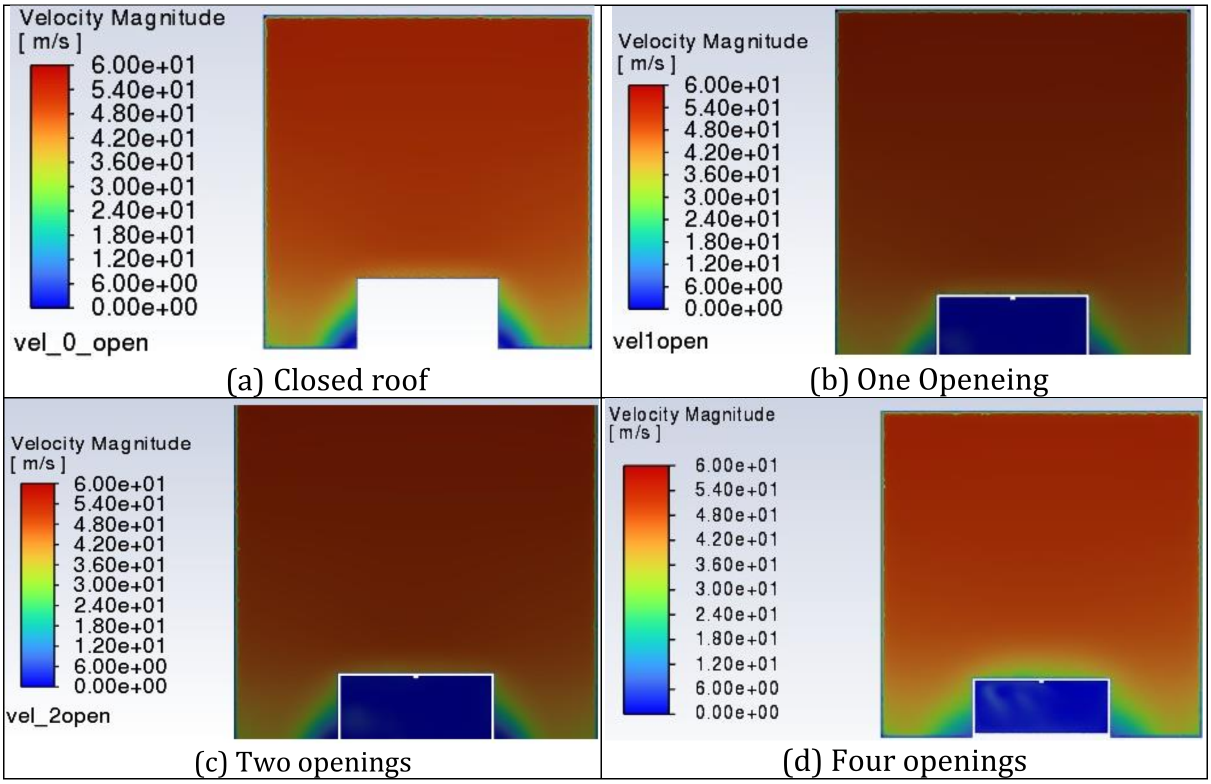

Figure 16. Velocity-magnitude contours for the closed and open roof configurations

The velocity contours show that the roof openings altered the local airflow pattern as well as the external flow above the roof. These changes were most visible near the opening edges and over the adjacent roof surface, particularly in the cases with two and four openings. The observed velocity variations agree qualitatively with the pressure contours in **Fig. 15** and provide further explanation for the pressure changes recorded around the roof openings.

3.4 Streamline and Wake Development for Different Opening Configurations

Fig. 17 shows how the airflow moved around and through the roof models. In every case, the flow left the surface near the windward roof edge and continued above the roof before entering the downstream region. This behavior agrees with the suction pattern shown previously in **Fig. 15**.

For the closed roof, the airflow passed only around the outside of the model. Behind the ridge, the streamlines formed a recirculating region that extended into the wake. Because the closed roof contained no openings, the internal space was isolated from the external airflow. After one or two openings were introduced, part of the flow passed through the roof, and the streamline pattern changed mainly around the opening edges. Local deflection of the streamlines was visible in these regions, together with changes in the nearby recirculating flow. Similar local variations were also evident in the pressure contours.

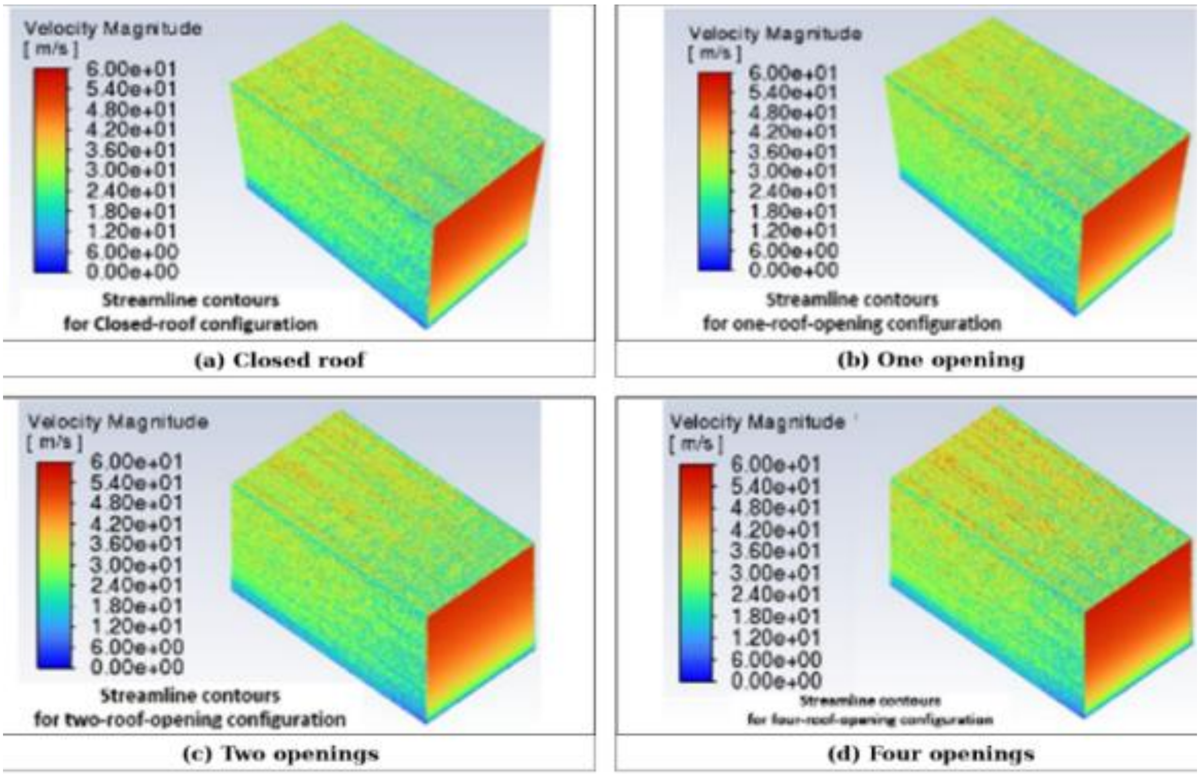

Figure 17. Streamline distributions for the investigated roof-opening configurations

With four roof openings, the streamline pattern departed most clearly from that of the closed model. Flow entered and left through several openings, producing local changes above the roof and within the downstream wake. The windward positive-pressure region remained visible, whereas the airflow over the roof was redirected in the vicinity of the openings.
Taken together, the streamline plots show that the openings changed the route followed by the air near the roof, particularly around the opening edges and in the downstream region.
The observed patterns are qualitatively consistent with the pressure and velocity contours presented in **Figs. 15** and **16** and support the aerodynamic interpretation of the investigated roof configurations **(Kopp et al., 2008; Blocken, 2014; Tominaga, 2024).**

3.5 CFD and Experimental Validation

The numerical predictions were compared directly with the wind-tunnel measurements at matching pressure-tap locations on the roof and wall surfaces. The same four roof-opening configurations were considered in both approaches. As illustrated in **Fig. 18**, the CFD data reproduced the overall variation observed experimentally for the closed roof and the roofs with one, two, and four openings.
The comparison gave R^2 = 0.996, RMSE ≈ 0.069, and ME ≈ 0.051. These values indicate close agreement between the measured and predicted pressure coefficients. Within the scope of the present study, the results show that the adopted numerical setup was capable of representing the principal mean-pressure trends across the investigated configurations. This agreement supports the suitability of the adopted domain, boundary conditions, mesh refinement, turbulence model, and pressure-coefficient extraction procedure for the present roof-opening configurations **(Tominaga et al., 2008; Richards and Norris, 2011; Li et al., 2025)**

3.6 Comparison with ASCE/SEI 7-22 Provisions

The measured pressure-coefficient (C_p) distributions obtained from the wind-tunnel experiments and the corresponding CFD simulations were interpreted with reference to the critical roof zones specified in ASCE/SEI 7-22 for low-rise buildings. The results showed that the locations of the highest suction, particularly near the windward roof edge and ridge-adjacent regions, were generally consistent with the critical roof zones identified by the code. However, the experimental and numerical results demonstrated that roof openings modified the local pressure distribution through enhanced internal–external airflow interaction and pressure redistribution, particularly for the two-opening and four-opening configurations. Consequently, validated wind-tunnel testing and CFD simulations can provide additional insight into localized aerodynamic effects that are not explicitly represented by the generalized roof-zone pressure coefficients specified in ASCE/SEI 7-22 **(ASCE, 2022; Kopp et al., 2008; Li et al., 2025).**

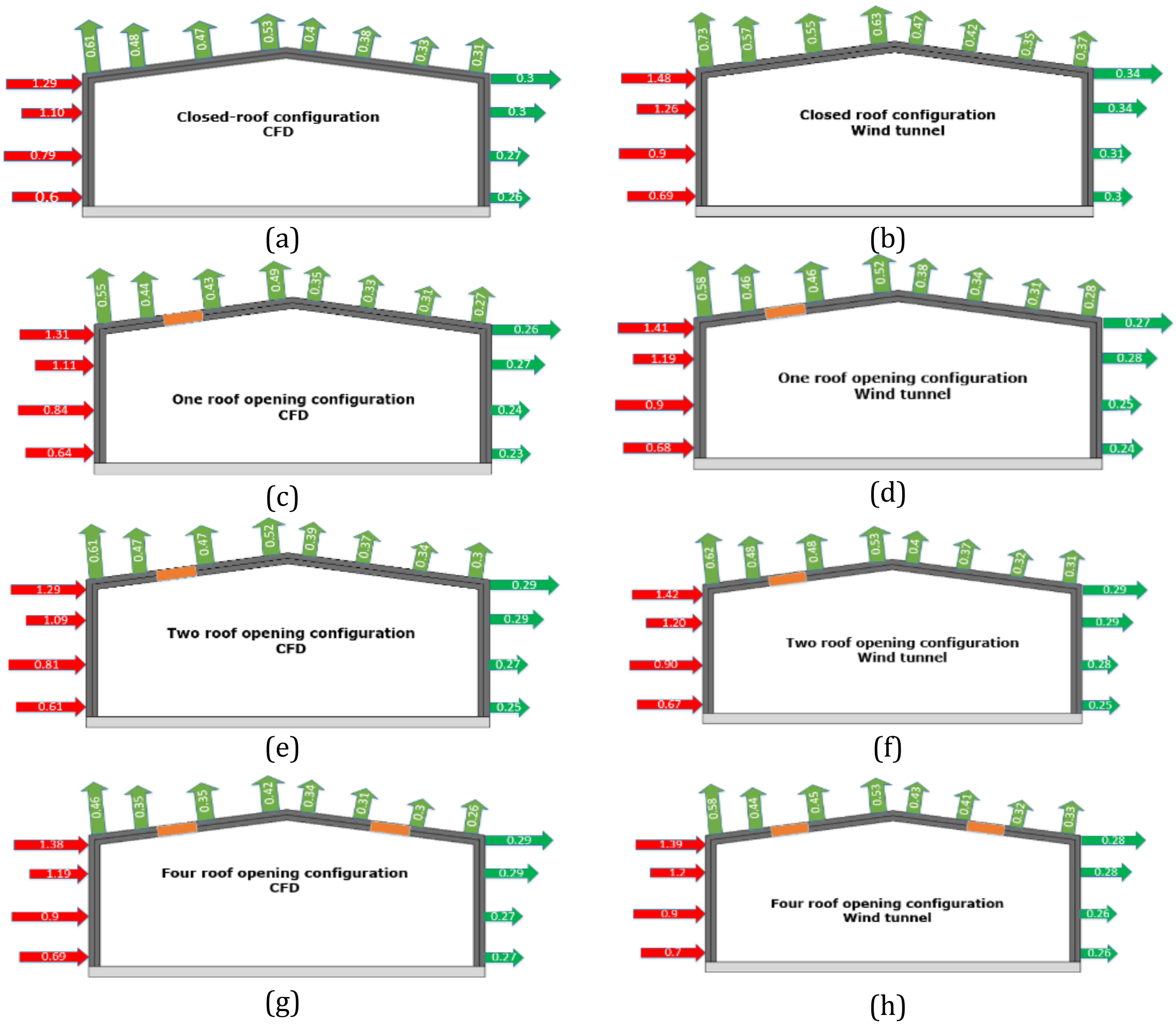

Figure 18. Comparison of CFD and wind-tunnel pressure-coefficient (Cp) distributions for the investigated roof-opening configurations.

4. CONCLUSIONS

The experimental and numerical results showed that the 8° gable roof produced the main aerodynamic features expected for a sharp-edged low-rise roof. Windward stagnation, roof-flow acceleration, suction over the inclined surfaces, separation near the roof edge, and wake formation were clearly observed. Peak suction occurred near the windward roof edge and in the region adjacent to the ridge. These areas therefore require particular attention when assessing pressures on roof cladding. Roof openings changed the pressure pattern mainly in the areas surrounding the openings and over the adjacent roof surface. These differences were limited in the one-opening case but became more noticeable when two and four openings were used. Among the examined cases, the four-opening model showed the largest departure from the closed-roof pressure distribution. The same local changes were visible in the velocity contours and streamline plots, especially near the opening edges and in the wake behind the model. Comparison with the wind-tunnel measurements gave R^2 = 0.996, RMSE ≈ 0.069, and ME ≈ 0.051. For the tested geometry and flow conditions, the results show that roof openings should be included when wind pressures are assessed for similar low-rise gable-roof buildings.

Acknowledgements

The authors acknowledge the Department of Civil Engineering and the Department of Aerospace Engineering, College of Engineering, University of Baghdad, for the wind tunnel facility and technical support.

Credit Authorship Contribution Statement

Ashraf Hameed Alsalmani: Conceptualization, methodology, experimental investigation, CFD simulation, analysis, visualization, and writing-original draft. Salah R. Al-Zaidee: Supervision, scientific guidance, validation, and writing-review and editing.

Declaration of Conflicting Interest

The authors declare that they have no known competing financial interests or personal relationships that could have influenced the work reported in this paper.

NOMENCLATURE

Symbol	Description	Symbol	Description
A_m	Projected frontal area of the model, m^2.	q	Dynamic pressure, Pa.
A_t	Wind-tunnel test-section area, m^2.	α	Roof slope angle, deg.
B	Building width, m.	β	Blockage ratio, %.
C_P	Pressure coefficient, dimensionless.	ε	Turbulence dissipation rate, m^2/s^3.
D	Building depth, m.	μ	Dynamic viscosity, Pa·s.
H	Characteristic building height, m.	ρ	Air density, kg/m^3.
k	Turbulent kinetic energy, m^2/s^2.	u_i	Velocity component, m/s.
P	Measured surface pressure relative to the reference pressure, Pa.	Re	Reynolds number, dimensionless.
		V	Reference wind velocity, m/s.

REFERENCES

Al Salmani, A.H., Al Zaidee, S.R., Al-Hasany, E.G., and Abdulhameed, S.A., 2019. Using BIM and virtual wind tunnel to investigate wind induced loads on steel agriculture buildings. *AUS*, 26(4), pp. 358–367. https://doi.org/10.33329/aus.2019.n26.4.49.

ANSYS Inc., 2025. ANSYS Fluent Theory Guide. Canonsburg, Pennsylvania, USA: ANSYS Inc.

ASCE, 2022. Minimum design loads and associated criteria for buildings and other structures. Reston, VA: American Society of Civil Engineers.

Aynsley, R.M., Melbourne, W.H., and Vickery, B.J., 1977. *Architectural Aerodynamics*. London: Applied Science Publishers.

Blocken, B., 2014. 50 years of computational wind engineering: past, present and future. *Journal of Wind Engineering and Industrial Aerodynamics*, 129, pp. 69–102. https://doi.org/10.1016/j.jweia.2014.03.008.

Cermak, J.E., 2003. Wind-tunnel development and trends in applications to civil engineering. *Journal of Wind Engineering and Industrial Aerodynamics*, 91(3), pp. 355–370. https://doi.org/10.1016/S0167-6105(02)00396-3.

Cook, N.J., 1985. *The Designer's Guide to Wind Loading of Building Structures*. London: Butterworths.

Demir, H., and Aktepe, B., 2025. Investigation on the effect of opening size and position on wind-driven cross-ventilation in an isolated gable roof building. *Applied Sciences*, 15(11), P. 6190. https://doi.org/10.3390/app15116190.

Dyrbye, C., and Hansen, S.O., 1997. *Wind Loads on Structures*. Chichester: John Wiley and Sons.

Ferziger, J.H., and Peric, M., 2002. *Computational Methods for Fluid Dynamics*. Berlin: Springer.

Fox, R.W., Pritchard, P.J., and McDonald, A.T., 2015. *Introduction to Fluid Mechanics*. Hoboken, NJ: Wiley.

Franke, J., Hellsten, A., Schlünzen, H., and Carissimo, B., 2007. *Best Practice Guideline for the CFD Simulation of Flows in the Urban Environment*. Brussels: COST Office.

Ginger, J.D., Holmes, J.D., and Kopp, G.A., 1997. Effect of building volume and opening location on internal pressures. *Journal of Wind Engineering and Industrial Aerodynamics*, 72, pp. 73–84.

Holmes, J.D., 2020. *Wind Loading of Structures*. 4th ed. Boca Raton: CRC Press.

Holmes, J.D., and Ginger, J.D., 2012. The gust wind speed duration in AS/NZS 1170.2. *Australian Journal of Structural Engineering*, 13, pp. 207–217. https://doi.org/10.7158/13287982.2012.11465111.

Kawai, H., and Nishimura, G., 1996. Characteristics of fluctuating suction and conical vortices on a flat roof in oblique flow. *Journal of Wind Engineering and Industrial Aerodynamics*, 60, pp. 211–225.

Kopp, G.A., Oh, J.H., and Inculet, D.R., 2008. Wind-induced internal pressures in houses. *Journal of Structural Engineering*, 134(7), pp. 1129–1138. https://doi.org/10.1061/(ASCE)0733-9445(2008)134:7(1129).

Lateb, M., Masson, C., Stathopoulos, T., and Bedard, C., 2013. Comparison of various types of k-epsilon models for pollutant emissions around a two-building configuration. *Journal of Wind Engineering and Industrial Aerodynamics*, 115, pp. 9–21. https://doi.org/10.1016/j.jweia.2013.01.001.

Launder, B.E., and Spalding, D.B., 1974. The numerical computation of turbulent flows. *Computer Methods in Applied Mechanics and Engineering*, 3, pp. 269–289. https://doi.org/10.1016/0045-7825(74)90029-2.

Lee, B.E., 1975. The effect of turbulence on the surface pressure field of a square prism. *Journal of Fluid Mechanics*, 69(2), pp. 263–282. https://doi.org/10.1017/S0022112075001437.

Li, M., Zhang, X., Bao, Y., Lin, J., Pei, C., Cheng, X., and Ma, C., 2025. The influence of roof opening and closure on the overall wind pressure distribution of airport terminal roof. *Buildings*, 15(5), P. 735. https://doi.org/10.3390/buildings15050735.

Melbourne, W.H., 1979. Turbulence effects on maximum surface pressures: a mechanism and possibility of reduction. *In Proceedings of the 5th International Conference on Wind Engineering, Fort Collins, Colorado, USA, pp. 541–552*. https://doi.org/10.1016/B978-1-4832-8367-8.50055-3.

Munson, B.R., Young, D.F., and Okiishi, T.H., 2013. *Fundamentals of Fluid Mechanics.* Hoboken, NJ: Wiley.

Murakami, S., 1997. Current status and future trends in computational wind engineering. *Journal of Wind Engineering and Industrial Aerodynamics*, 67–68, pp. 3–34. https://doi.org/10.1016/S0167-6105(97)00230-4.

Nozawa, K., and Tamura, T., 2002. Large eddy simulation of the flow around a low-rise building immersed in a rough-wall turbulent boundary layer. *Journal of Wind Engineering and Industrial Aerodynamics*, 90(10), pp. 1151–1162. https://doi.org/10.1016/S0167-6105(02)00228-3.

Palutikof, J.P., Brabson, B.B., Lister, D.H., and Adcock, S.T., 1999. A review of methods to calculate extreme wind speeds. *Meteorological Applications*, 6(2), pp. 119–132. https://doi.org/10.1017/S1350482799001103.

Richards, P.J., and Hoxey, R.P., 1993. Appropriate boundary conditions for computational wind engineering models using the k–ε turbulence model. *Journal of Wind Engineering and Industrial Aerodynamics*, 46–47, pp. 145–153. https://doi.org/10.1016/0167-6105(93)90124-7.

Richards, P.J., and Norris, S.E., 2011. Appropriate boundary conditions for computational wind engineering models revisited. *Journal of Wind Engineering and Industrial Aerodynamics*, 99(4), pp. 257–266. https://doi.org/10.1016/j.jweia.2010.12.008.

Simiu, E., and Scanlan, R.H., 1996. *Wind Effects on Structures*. New York: John Wiley and Sons.

Solari, G., 1993. Gust buffeting. I: peak wind velocity and equivalent pressure. *Journal of Structural Engineering*, 119(2), pp. 365–382. https://doi.org/10.1061/(ASCE)0733-9445(1993)119:2(365).

Stathopoulos, T., 1984. Wind loads on low-rise buildings: A review of the state of the art. *Journal of Wind Engineering and Industrial Aerodynamics*, 9, pp. 119–135.

Tamura, T., 2008. Towards practical use of LES in wind engineering. *Journal of Wind Engineering and Industrial Aerodynamics*, 96(10–11), pp. 1451–1471. https://doi.org/10.1016/j.jweia.2008.02.034.

Tieleman, H.W., 2003. Wind tunnel simulation of wind loading on low-rise structures: A review. *Journal of Wind Engineering and Industrial Aerodynamics*, 91(12–15), pp. 1627–1649. https://doi.org/10.1016/j.jweia.2003.09.021.

Tominaga, Y., Mochida, A., Yoshie, R., Kataoka, H., Nozu, T., Yoshikawa, M., and Shirasawa, T., 2008. AIJ guidelines for practical applications of CFD to pedestrian wind environment around buildings. *Journal of Wind Engineering and Industrial Aerodynamics*, 96(10–11), pp. 1749–1761. https://doi.org/10.1016/j.jweia.2008.02.058.

Versteeg, H.K., and Malalasekera, W., 2007. *An Introduction to Computational Fluid Dynamics*. Harlow: Pearson.

White, F.M., 2016. *Fluid Mechanics*. New York: McGraw-Hill Education.

دراسة الضغط المستحث بالرياح على سقف جملوني منخفض الميل بزاوية 8 درجات باستخدام الفحوصات المختبرية والمحاكاة العددية

أشرف حميد خلف السلماني [1، 2، *]، صلاح رحيمه الزيدي[2]

[1] مكتب رئيس مجلس النواب العراقي، بغداد، العراق
[2] قسم الهندسة المدنية، كلية الهندسة، جامعة بغداد، بغداد، العراق

الخلاصة

يهدف هذا البحث إلى دراسة الضغوط المستحثة بالرياح على سقف جملوني منخفض الميل بزاوية 8 درجات باستخدام اختبارات نفق الرياح والمحاكاة العددية ببرنامج ANSYS Fluent. يمثل السقف المدروس أحد أشكال أسقف المباني المنخفضة الارتفاع وفق تصنيف ASCE/SEI 7. تم فحص أربع حالات للسقف، شملت السقف المغلق، والسقف ذي فتحة واحدة، والسقف ذي الفتحتين، والسقف ذي الأربع فتحات. أجريت الاختبارات المختبرية تحت الظروف نفسها داخل نفق رياح مفتوح الدائرة في كلية الهندسة، جامعة بغداد، وبسرعة رياح مرجعية ثابتة مقدارها 38 م/ثا. تم قياس الضغوط السطحية باستخدام نقاط ضغط موزعة على الجدار المواجه للرياح، والجدار الخلفي، وسطوح السقف الجملوني، ثم حُسبت معاملات الضغط المناظرة. كما تم بناء نموذج عددي ثلاثي الأبعاد باستخدام صياغة RANS للجريان المستقر غير القابل للانضغاط في ANSYS Fluent 2025 R1مع نموذج الاضطراب القياسي k–ε. أظهرت النتائج أن زيادة عدد الفتحات في السقف أدت إلى تعزيز التفاعل بين الجريان المنفصل الخارجي والحجم الهوائي الداخلي، مما سبب إعادة توزيع واضحة للضغط على سطح السقف. كما أظهرت نتائج المحاكاة العددية توافقاً جيداً جداً مع القياسات المختبرية، إذ بلغت قيمة معامل التحديد$R^2 = 0.996$ ، بينما بلغت $RMSE \approx 0.069$و $ME \approx 0.051$. وتشير النتائج إلى أن فتحات السقف تؤثر بشكل ملحوظ في الاستجابة الديناميكية الهوائية لضغوط الرياح على الأسقف الجملونية المنخفضة الارتفاع، لذلك ينبغي أخذها بنظر الاعتبار عند تقييم ضغوط الرياح المؤثرة على الأسقف.

الكلمات المفتاحية: اختبار نفق الرياح، السقف الجملوني، الضغط المستحث بالرياح، فتحات السقف، هندسة الرياح.